Available online at www.sciencedirect.com
SCIENCE DIRECT®
Journal of volcanology and geothermal research
ELSEVIER
Journal of Volcanology and Geothermal Research xx (2005) xxx–xxx
www.elsevier.com/locate/jvolgeores

Eruption of the dacite to andesite zoned Mateare Tephra, and associated tsunamis in Lake Managua, Nicaragua

Armin Freundt [a,b,*], Steffen Kutterolf [a], Heidi Wehrmann [a], Hans-Ulrich Schmincke [a,b], Wilfried Strauch [c]

[a] *SFB 574 at Kiel University, Wischhofstr. 1-3, D-24148 Kiel, Germany*
[b] *IfM-GEOMAR, Wischhofstr. 1-3, D-24148 Kiel, Germany*
[c] *INETER, Managua, Nicaragua*

Received 1 February 2005; received in revised form 14 June 2005; accepted 20 June 2005

Abstract

The dacite to andesite zoned Mateare Tephra is the fallout of a predominantly plinian eruption from Chiltepe peninsula at the western shore of Lake Managua that occurred 3000–6000 years ago. It comprises four units: Unit A of high-silica dacite is stratified, ash-rich lapilli fallout generated by unsteady subplinian eruption pulses affected by minor water access to the conduit and conduit blocking by degassed magma. Unit B of less silicic dacite is well sorted, massive pumice lapilli fallout from the main, steady plinian phase of the eruption. Unit C is andesitic fallout that is continuous from unit B except for the rapid change in chemical composition, which had little influence on the ongoing eruption except for a minor transient reduction of the discharge rate and access of water to the conduit. After this, discharge rate re-established to a strong plinian eruption that emplaced the main part of unit C. This was again followed by water access to the conduit which increased through upper unit C. The lithic-rich lapilli to wet ash fallout of unit D is the product of the fully phreatomagmatic terminal phase of the eruption. A massive well-sorted sand layer, the Mateare Sand, replaces laterally variable parts of unit A and lowermost part of unit B in outcrops up to 32 m above present lake level. The corresponding interval missing in the primary fallout can be identified by comparing the composition of pumice entrained in the sand, and pumice from the local base of unit B on top of the sand, with the compositional gradient in undisturbed fallout. The amount of fallout entrained in the sand decreases with distance to the lake. The Mateare Sand occurs at elevations well above beach levels and its widespread continuous distribution defies a fluviatile origin. Instead, it was produced by lake tsunamis triggered by eruption pulses during the initial unsteady phase of activity. Such tsunamis could threaten areas not affected by fallout, and represent a hazard of particular importance in Nicaragua where two large lakes host several explosive volcanoes.

Keywords: plinian eruption; compositional zonation; tsunami; volcanic hazards

* Corresponding author. IfM-GEOMAR, Wischhofstr. 1-3, D-24148 Kiel, Germany. Tel.: +49 431 600 2131; fax: +49 431 600 2924.
E-mail address: afreundt@ifm-geomar.de (A. Freundt).

0377-0273/$ - see front matter © 2005 Elsevier B.V. All rights reserved.
doi:10.1016/j.jvolgeores.2005.06.001

1. Introduction

1.1. Volcanogenic tsunamis

Tsunamis are long waves triggered by the sudden displacement of water by mass movement at the seafloor. Tsunamigenic mass movements can be seismic events that offset the seafloor or submarine landslides (e.g., Harbitz, 1992; Bourgeois et al., 1999; von Huene et al., 2003) but also subaerial landslides and pyroclastic flows that enter the sea (Keating and McGuire, 2000; Self et al., 1984; Sigurdsson and Carey, 1989; Waythomas and Neal, 1998; McCoy and Heiken, 2000; Carey et al., 2001; De Lange et al., 2001; Freundt, 2003, in press). Tsunamis on the open sea have long wavelengths, low amplitudes, and travel at great speed depending on water depth. When these waves slow down in shallowing coastal waters their amplitude grows dramatically with a devastating effect on flooded coastal areas. Reported maximum tsunami runup heights include 326 m asl on Lanai (Moore and Moore, 1984), >400 m asl at Kohala on Hawaii (McMurtry et al., 2004), and 500 m asl at Lituya Bay, Alaska (Miller, 1960). Tsunamis of volcanic origin may be formed by earthquakes accompanying eruption, caldera subsidence, submarine explosions, and pyroclastic flows, landslides, avalanches and lahars entering the sea or moving under water (Latter, 1981), and several such processes may act simultaneously.

Most documented tsunamis occurred in the ocean and few reports exist on volcanogenic tsunamis in lakes. Voight et al. (1981) describe water runup to 260 m above Spirit Lake upon impact of the avalanche from the collapse of Mt. St. Helens' north flank at the beginning of the May 18, 1980, eruption. Belousov et al. (2000) report 2–30 m runup heights of tsunamis generated by subaquatic explosions during surtseyan eruptions in Lake Karymskoye, Kamchatka, in 1996. They also describe minor waves coupled to radially expanding surges.

The risk from volcanogenic lake tsunamis is particularly high in Nicaragua, where the most densely populated areas lie along the shores of Lake Managua and Lake Nicaragua, which together cover 10% of the country's area. These lakes lie within the active subduction-related volcanic arc. Although there have been speculations about lake tsunamis possibly formed by volcano-flank collapse at Mombacho volcano (Vallance et al., 2001) or pyroclastic flows from Apoyo caldera (Sussman, 1985), we here present the first documented case of an eruption-generated tsunami in Lake Managua.

1.2. Central Nicaraguan succession of widespread tephras

We have recently revised and extended the stratigraphy and ^{14}C dating of deposits of highly explosive eruptions from arc volcanoes in west-central Nicaragua, building on earlier work by Bice (1985) and references therein. The stratigraphic succession at the western shore of Lake Managua (Fig. 1) comprises the Chiltepe Formation (CF), including six tephras younger than 15 ka from plinian and phreatomagmatic eruptions on Chiltepe peninsula, and the newly identified Mateare Formation (MF) underneath a major regional unconformity, which is composed of numerous basaltic to dacitic lapilli-fallout and tuff deposits (Fig. 2). Chiltepe peninsula is a volcanic complex hosting the Apoyeque stratocone, the Xiloa maar, mafic cinder cones and tuff rings, and at least two other vent sites that are no longer visible. Highly explosive eruptions occurred at a relatively high and steady frequency during the recent past and will most probably continue at the Chiltepe volcanic complex. This emphasizes the need to understand its eruptive history and mechanisms to assess future volcanic hazards. In this contribution we focus on the eruption of the Mateare Tephra and its associated tsunami.

The Mateare Tephra is underlain by the phreatomagmatic dacitic Xiloa Tephra, which consists of two white pyroclastic-surge ash deposits (Xiloa A and C) bracketing a central ash-rich, normally graded pumice fallout layer (Xiloa B). Carbonized wood contained in the Xiloa Tephra yields a ^{14}C age of 6105 ± 30 a B.P. (Fig. 2). The dacitic plinian Chiltepe Tephra was produced by the youngest plinian eruption from the Chiltepe volcanic complex. In the area west of Managua City, the distal Chiltepe Tephra overlies the Masaya Triple Layer, a basaltic plinian fallout from Masaya caldera (Williams, 1983; Perez and Freundt, in press). Plant remains within the Masaya Triple Layer yield a radiocarbon age of 2120 ± 120 a B.P. These dates constrain the age of the Mateare Tephra to between 3000 to 6000 years ago.

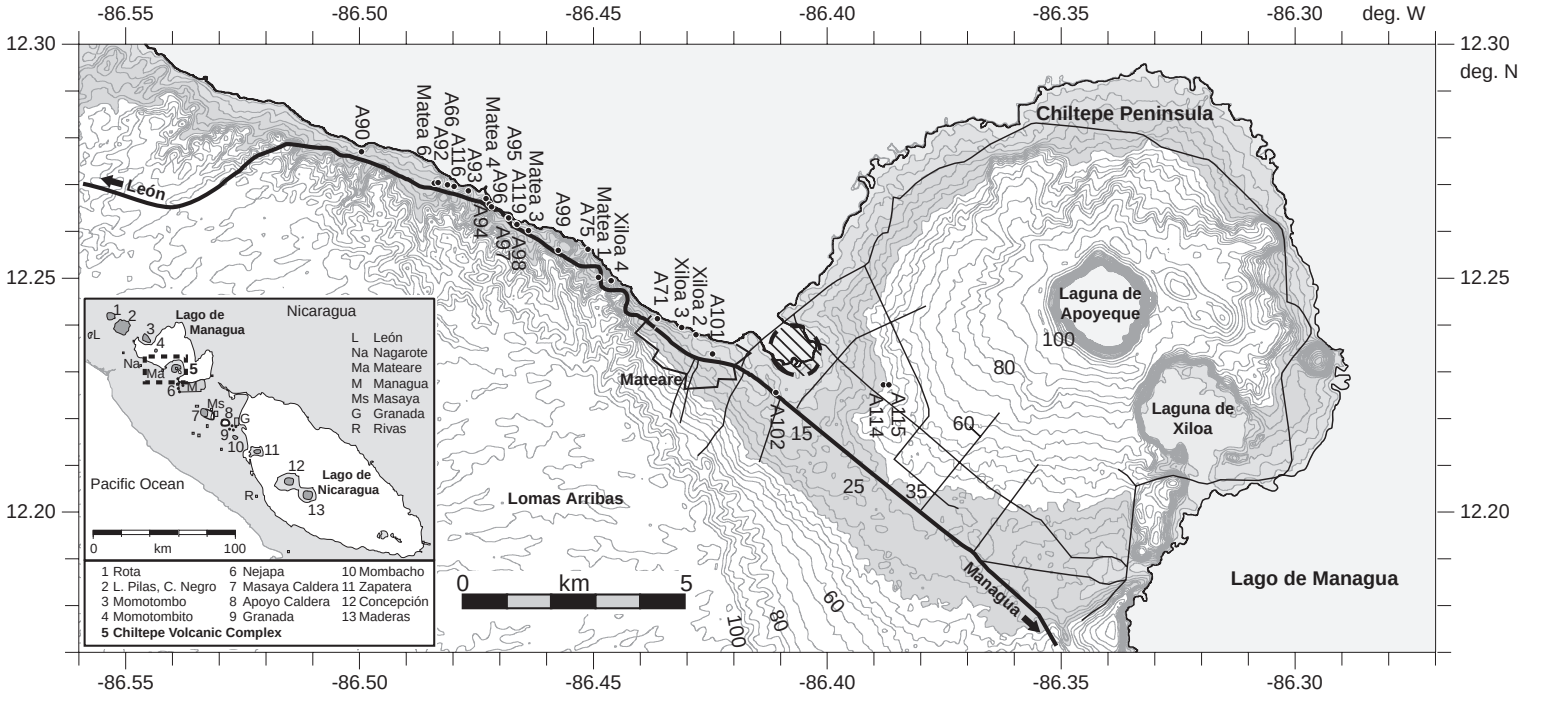

Fig. 1. Map of the western shore of Lake Managua around the town of Mateare and the Chiltepe peninsula hosting Apoyeque and Xiloa volcanoes. Contours at 5 m intervals taken from digital elevation model; numbers give elevation [m] above lake. Gray shading highlights lowlands <30 m above present lake level. Hatched circle marks possible vent site of Mateare eruption. Inset map of west-central Nicaragua with chain of arc volcanoes intersecting Lake Managua and Lake Nicaragua. Dashed frame shows position of the large map.

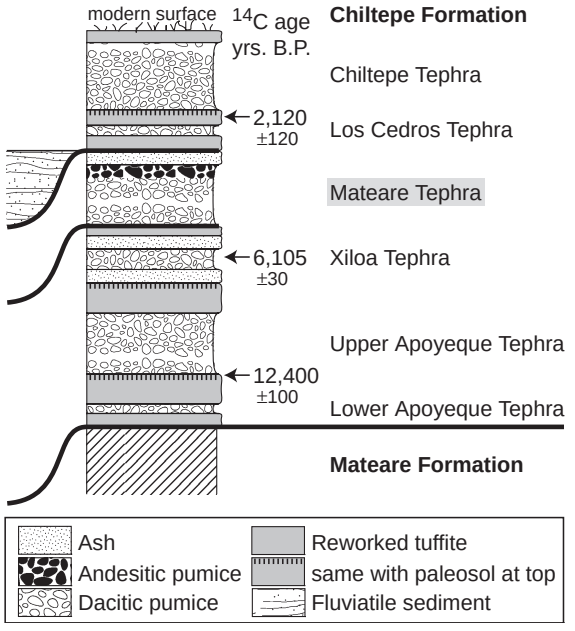

Fig. 2. Schematic columnar section of the Chiltepe Formation which comprises six tephras less than 15 ka old. ^{14}C-ages are from paleosol below Upper Apoyeque Tephra, charcoal within Xiloa Tephra, and plant remains within the Masaya Triple Layer which underlies Chiltepe Tephra west of Managua City. Bold lines indicate major erosional unconformities. The most prominent unconformity separates the Chiltepe Formation from the Mateare Formation, which is still undated. Extensive erosional channels formed after the Mateare Tephra are filled with fluviatile sediments several meters thick.

In part 1 of this paper we characterize the eruption of the Mateare Tephra and its compositional zonation. In part 2 we describe the tsunami deposit and use results from part 1 to determine the timing of tsunami formation in the course of the eruption as well as the effects of tsunamis on the primary fallout deposit.

2. Part 1: the Mateare Tephra

2.1. Lithology of the deposit

The Mateare Tephra is exposed along the western shore of Lake Managua (Fig. 1). A thin incipient paleosol separates the Mateare Tephra from the Xiloa Tephra in some outcrops but commonly the boundary is an erosional unconformity covered by water-emplaced sand deposits, the Xiloa and Mateare Sands described below. The top of the Mateare Tephra is commonly eroded and covered by channelized fluviatile sediments and reworked tuffite with a paleosol on top. The tuffite contains the commonly <50-cm-thick Los Cedros pumice fallout layer which has survived erosion at only a few locations. The paleosol-top of the tuffite is overlain by the Chiltepe Tephra.

From bottom to top, we distinguish four units within the Mateare Tephra: dacitic pumice units A and B, andesitic pumice unit C, and tuff D at the top (Fig. 3a). A complete section, however, is only found at two outcrops (A114 and A71 in Fig. 1). Post-eruptive erosion has removed units D and C at places whereas syn-eruptive erosion—as discussed below—has removed unit A almost everywhere along the shores of Lake Managua. In most outcrops, therefore, the Mateare Tephra is only represented by the about 2-m-thick massive fallout pumice unit B, which is sometimes capped by remains of unit C, and resting on the undulating surface of the underlying Mateare Sand (Fig. 3b).

Unit A at locality A114 (Fig. 1) is a 30-cm-thick well-stratified package of seven normally graded, ash-rich beds of light gray angular dacitic pumice lapilli (Fig. 3c). At outcrop A71, 5 km to the NW, the seven-layer package reaches only 16 cm in thickness and is accordingly finer in grain size. At both localities, the primary fallout is then interrupted by a wavy erosional unconformity capped by the Mateare Sand upon which rests unit B.

Massive pumice fallout *unit B* consists of very well sorted, angular, dacitic pumice clasts (Fig. 3a, b). At locality A114, however, the lower third of its thickness is weakly reversely graded and contains abundant outsized pumice bombs. The dominant light gray highly vesicular pumice lapilli are characterized by small bubbles. Upward through the bed an increasing number of larger, more coarsely vesicular, pink pumices occur dispersed in the light gray pumice. Some angular, dense, black obsidian chips <1.5 cm in size occur in the lapilli-size fraction. A few percent lithic fragments are dense dacitic lava, which is dominantly pale gray and unaltered but minor red-brown hydrothermally altered clasts also occur. In several outcrops near the town of Mateare the base of unit B is formed by a 1–5 cm thick, well bedded fine-lapilli to coarse-ash layer B1 which thickens in the

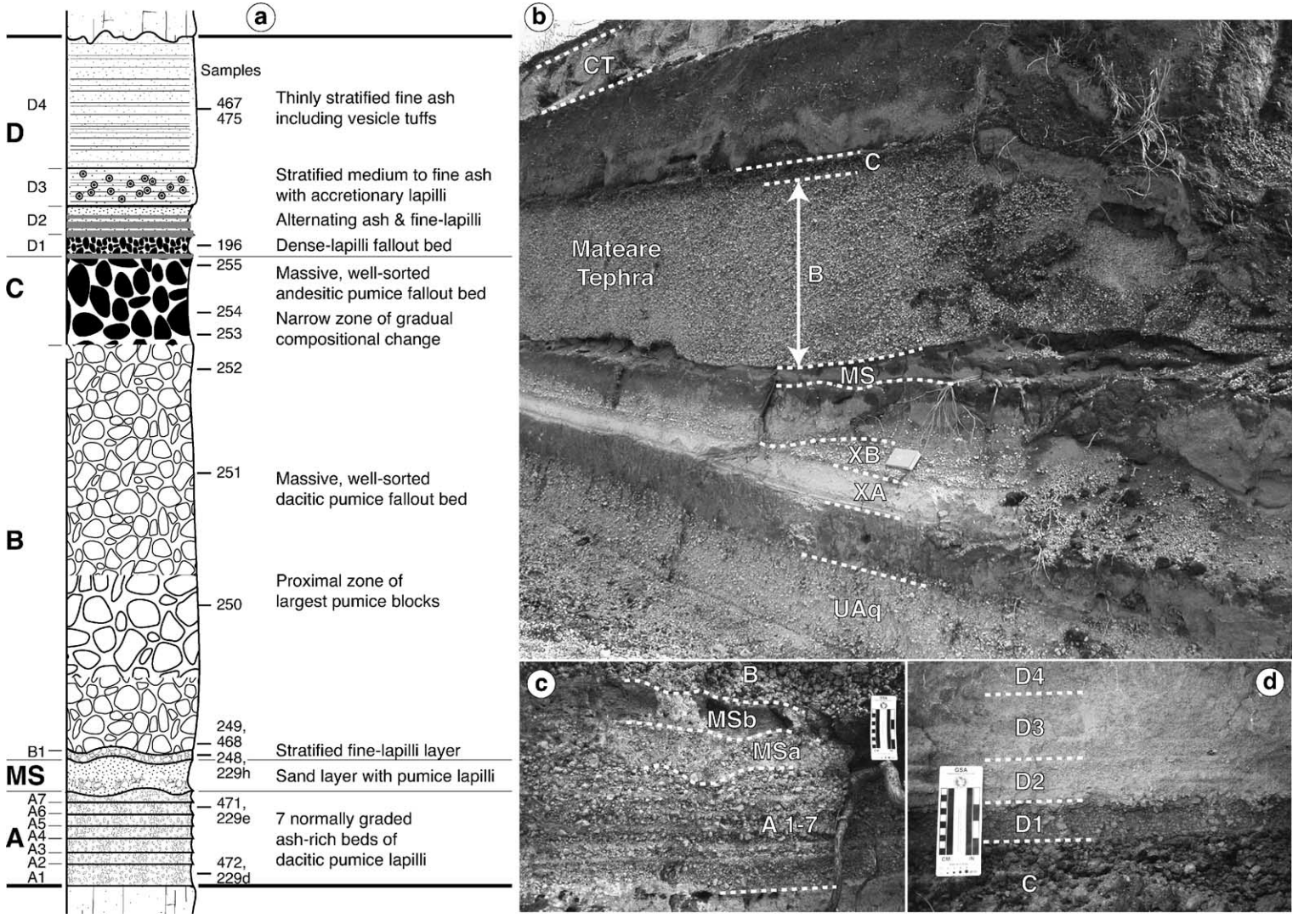

Fig. 3. (a) Composite profile of the Mateare Tephra, composed of units A through D, and the intercalated Mateare Sand (MS). (b) Photograph of Loc. A96 showing the common appearance of the Mateare Tephra: MS is overlain by unit B, which is in turn capped by partly eroded unit C. Upper Apoyeque Tephra (UAq) at bottom is capped by tuffite with a paleosol on top, followed by the Xiloa Tephra units A and B (XA, XB), the latter being partly eroded while Xiloa unit C is completely missing at this location. Lahar-like tuffite separates XB from MS. (c) Photograph of bedded unit A (beds A1–7) of the Mateare Tephra at Loc. A114. Lapilli-rich MSa and sandy MSb are two layers of the Mateare Sand at this outcrop. (d) Photograph of Mateare Tephra unit D (layers D1–4) on top of unit C at Loc. A115.

troughs of the sand-layer surface. This fine-lapilli layer is rich in obsidian and lithic fragments.

The ~20-cm-thick *unit C* is composed of dark gray and black andesitic pumice (Fig. 3b). The change in color and composition from unit B to unit C is gradual in that light gray pumice is mixed with an upward increasing fraction of darker pumice across a narrow thickness interval. There is no depositional boundary indicative of a break in the fallout emplacement. Grain size, however, decreases somewhat across the upper 10 cm of unit B and then rapidly increases across the base of unit C, which is symmetrically graded with maximum grain size at the center. The decrease in grain size across the upper half of unit C is associated with a decrease in pumice porosity.

A thin ash veneer separates unit C from the overlying *unit D* which begins with layer D1 (7 cm thick at A114, Fig. 3d), a moderately sorted bed of poorly vesicular to dense dark-gray andesitic lapilli, some light-gray vesicular pumice and dense black obsidian fragments, and abundant lithic lava fragments. Layer D2 is 9 cm thick, planar bedded, and consists of an alternating sequence of three fine-lapilli and three fine-to-medium ash beds. Stratified fine to medium ash with a very high concentration of accretionary lapilli forms the 12-cm-thick layer D3. Layer D4 is 42 cm of very thinly stratified fine ash containing several vesicle-tuff horizons, and is erosively overlain by reworked tuffite.

2.2. Areal distribution and source vent

Isopach and isopleth maps of the Mateare Tephra (Fig. 4) are poorly constrained since all outcrops lie within a 1-km-wide NW–SE-trending belt along the western shore of Lake Managua (Fig. 1). The maximum pumice and lithic grain sizes decrease systematically toward the NW (Fig. 5a), consistent with increasing distance from vent. The upper envelope of the thickness data of the Mateare Tephra (Fig. 5b), considering only locations where the andesitic unit C is at least partly present and hence post-eruptive erosion was limited, indicates thinning toward the NW. However, even where unit C is present, there is considerable variation in thickness of units B + C between neighboring outcrops (Fig. 5b) and this variation is particularly large at outcrops closer to the lake shore (Fig. 5c). This feature will be discussed further below. The thickness distribution allows a conservative estimate of an erupted tephra volume of ~1 km^3, corresponding to 10^{12} kg DRE magma of which 90% is dacitic in composition.

A high-resolution (1 m) digital elevation model (DEM) of the western shore of Lake Managua and Chiltepe peninsula reveals a shallow, circular, ~1.5-km-diameter depression on the NW-shore of the peninsula east of the town of Mateare, which is now covered by younger deposits. We interpret this depression as the vent site of the Mateare eruption (Figs. 1 and 4) for three reasons: (1) It would be compatible with the variations of thickness and grain size along the locations to the NW. (2) The overall coarse grain size, the presence of many outsized (possibly ballistic) pumice bombs, but relatively low thickness at outcrop A114 suggest this is a near-vent but off-axis location. (3) The Mateare Tephra does not occur in exposures of the relevant stratigraphic section at the northern part of Chiltepe peninsula, within Apoyeque crater, and near Xiloa maar, as would be expected from a vent site at the central or eastern regions of the peninsula.

2.3. Vertical changes in pumice composition

Chemical variations in the Mateare Tephra are illustrated by the total alkali–silica (TAS) and Ba–Zr diagrams in Fig. 6. Bulk-rock chemical compositions reported here were obtained from X-ray fluorescence (XRF) analyses of bulk samples of at least ten pumice lapilli randomly picked at each level; single-lapillus analyses were only made for unit D and obsidian fragments. The Mateare Tephra is chemically (and mineralogically) distinct from the other eruptive products of the Chiltepe volcanic complex. Bedded unit A represents the most evolved, first-erupted dacite of rather uniform composition. The dominant light gray and the subordinate pinkish pumice clasts of unit B overlap in their less-silicic dacitic compositions. Unit B shows a weak increase upwards in silica and incompatible elements (Fig. 7). The dark unit C contains andesitic pumice changing upward from 60 to 57 wt.% SiO_2 (Fig. 7). Unit D on top mainly contains poorly vesicular low-SiO_2 andesitic lapilli compositionally corresponding to the top of unit C as well as moderately vesicular lapilli from lower unit C and vesicular pumice from unit B.

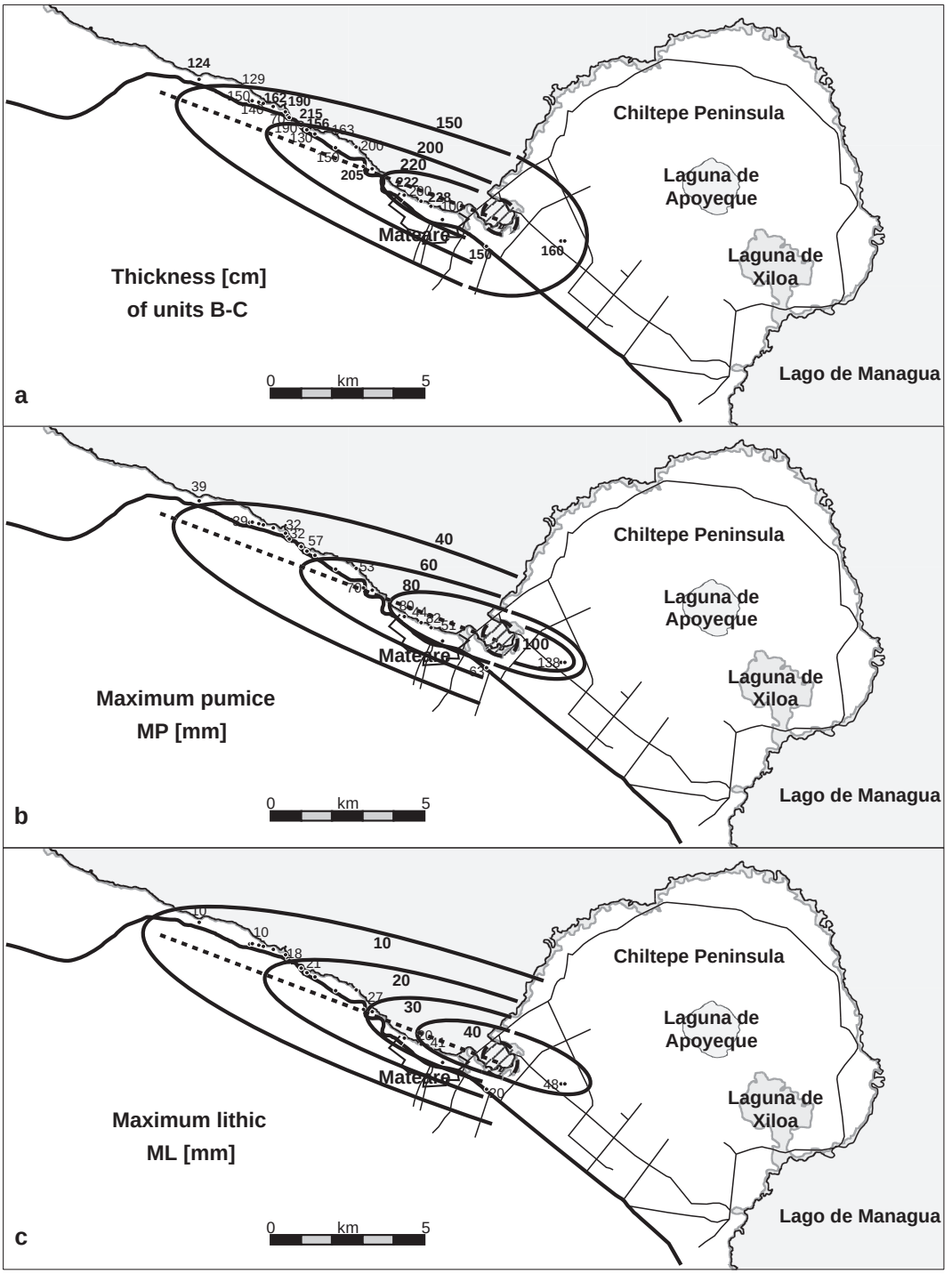

Fig. 4. Isopach and isopleth maps for the Mateare Tephra (units B and C combined). Map sections are identical to Fig. 1. Dotted lines are the distribution axes pointing WNW. MP, ML are averages of the mean diameters of the five largest clasts per outcrop.

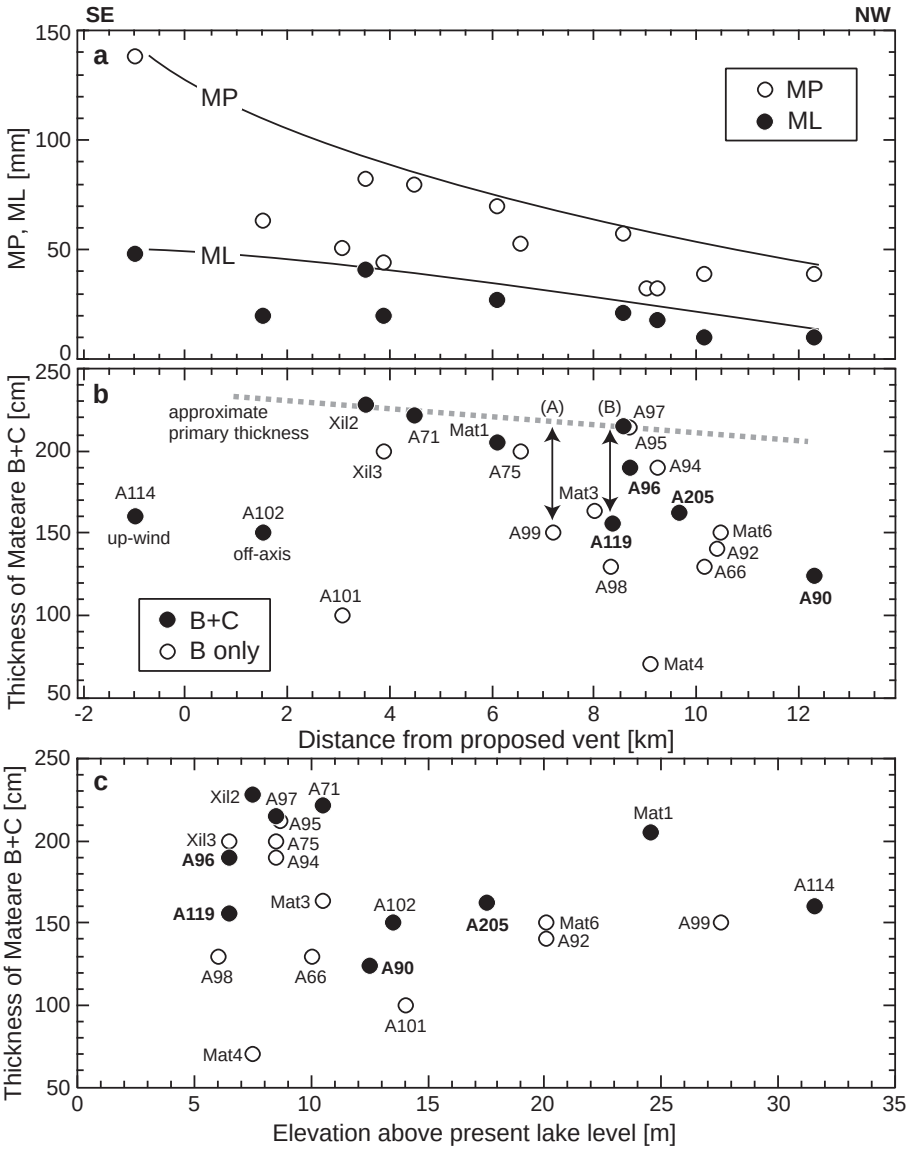

Fig. 5. (a) Maximum grain size of pumice (MP) and lithics (ML) and (b) thickness of fallout units B+C versus distance from the proposed vent site. Lines in (a) envelope the MP and ML data. Dashed line in (b) indicates approximate along-axis thickness variation. (c) Thickness of fallout deposit (B+C) versus elevation above lake level. Bold locality labels (A90, A96, A119, A205) facilitate comparison between (b) and (c) of localities where unit C is present, yet thickness is reduced. Double-arrows in (b) exemplify (A) ~60 cm thickness missing due to post-eruptive erosion at A99, and (B) ~50 cm thickness missing at A119 due to initial unit-B fallout entrained in the Mateare Sand.

Vertical compositional variation through the Mateare Tephra shows two inflection points where the gradient steepens abruptly at the A/B and B/C boundaries (Fig. 7). These inflections reflect gaps between the compositional ranges of the three units (Fig. 6). The width of the compositional gap between units A and B varies between outcrops because the composition in the most basal pumice of unit B varies (Fig. 7). This suggests that the basal pumices and hence the contact between unit B and the underlying sand are not time-equivalent between outcrops as discussed further below.

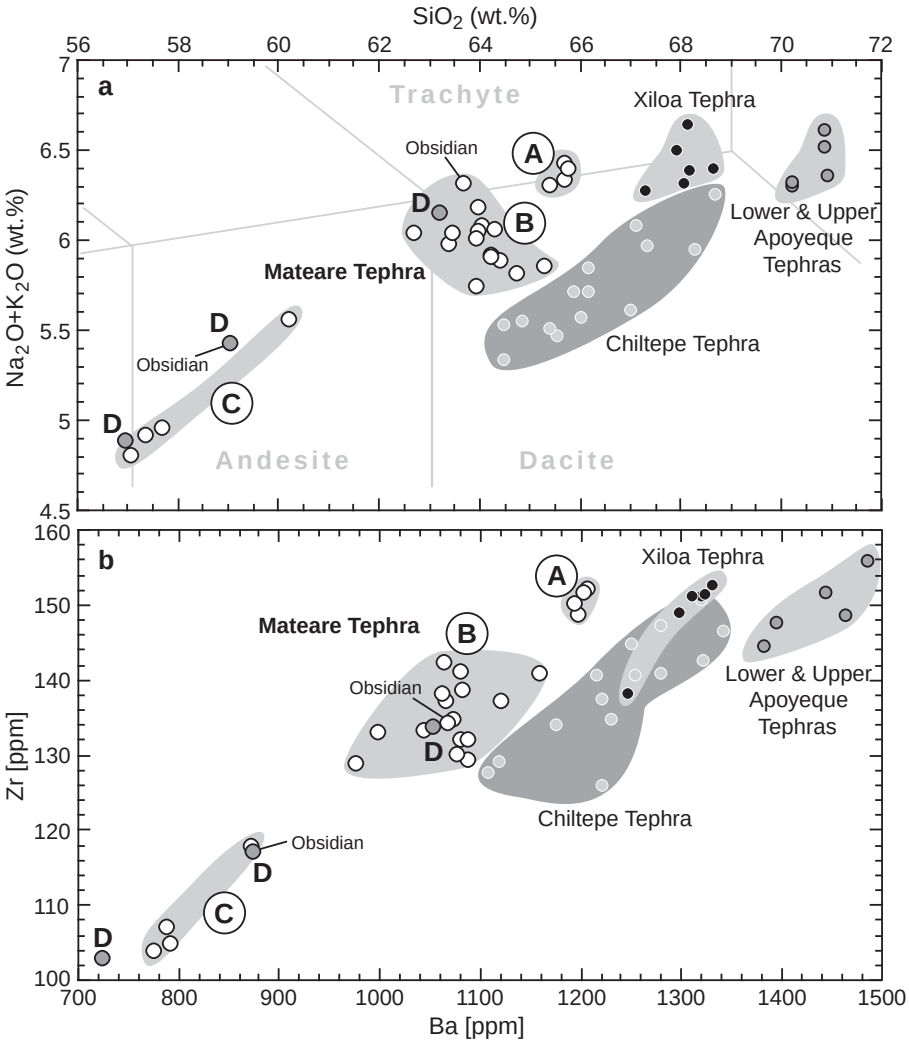

Fig. 6. (a) Total alkalis versus silica variation and (b) Zr over Ba variation of units A, B, C (marked areas) and D (dark-gray dots) of the Mateare Tephra. Data fields for Chiltepe, Xiloa and Lower and Upper Apoyeque Tephras are included for comparison. Data were obtained by XRF analyses of bulk samples of 10–15 pumice lapilli. Concentrations are normalized to anhydrous composition. An obsidian fragment in unit B has the composition of its hosting pumice whereas another obsidian fragment in layer D1 has the composition of unit-C pumice.

2.4. Vertical changes in pumice texture

We determined the average bulk density of 30–40 g of pumice lapilli of the -4Φ to -3Φ size fractions by weighting a 280 ml cup filled to the brim with the lapilli and well-sorted sand of pre-determined loose-packed bulk density. We used a pygnometer filled with water and ground pumice powder to determine the solid density. The resulting average pumice porosity (Fig. 7) increases upward from unit A (64–68 vol.%) to the center of unit B (77 vol.%) and then decreases to the base of unit C (66 vol.%). In unit C, porosity first increases to 74 vol.% and then drops steeply through the top of unit C (61 vol.%) to unit D (40 vol.%). Porosity at the base of unit B varies between outcrops (68–78 vol.%), reflecting the observed compositional variation since higher porosity roughly correlates with decreasing Zr and other incompatible element concentrations. Moreover, the variation in porosity across units B and C roughly

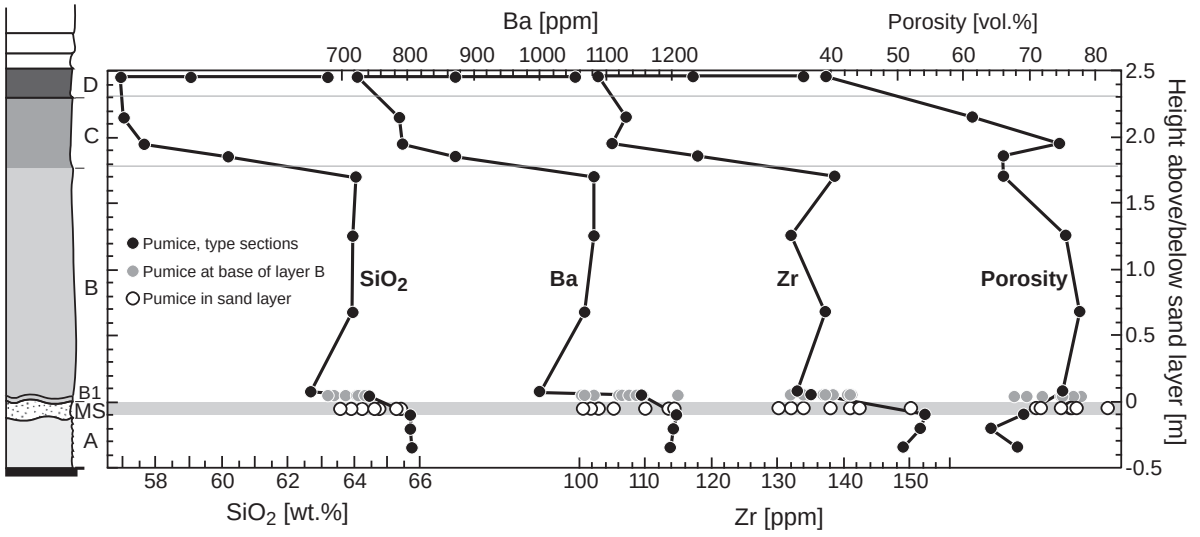

Fig. 7. Vertical variations in the concentrations of selected elements (SiO_2, Ba, Zr) and average pumice porosity through the Mateare Tephra.

correlates with the grain-size variation in that levels of lower vesicularity also have smaller lapilli sizes.

The vesicle texture of pumice lapilli in unit A is characterized by small, round, closely packed vesicles. Upward through unit B the vesicle size range of pumice lapilli widens to larger vesicles. Pumice lapilli contain increasing portions in which vesicles are strongly stretched and viscously deformed. This texture predominates in pumice at the top of unit B. Stretched zones diminish through the base of unit C, where pumice contains a heterogenous mixture of moderately porous zones of small vesicles and highly porous zones of large vesicles. The highly vesicular pumice at the center of unit C contains zones where densely packed vesicles are separated by only very thin glass walls. At the top of unit C, juvenile clasts have a scoriaceous texture of irregularly shaped, crenulate bubbles separated by thick walls. Lapilli in unit D either have a moderate to low-porosity scoriaceous texture or are dense and microcrystalline.

2.5. Vertical changes in ash components

Ash particles of the 0 Φ-size fraction were analyzed petrographically and chemically because they reveal some features not observable in the lapilli-size fractions. Lithic ash particles consist of various lava and scoria fragments with mineral assemblages dominated by plagioclase and occasional orthopyroxene. Such lithics range from dark-brown sideromelane with black patches and >50 vol.% microlites to microcrystalline dark-brown to dark-gray fragments, some with flow-aligned plagioclase laths. They seem to be mostly derived from andesitic and basaltic lava bodies. Fragments of dacitic lava are (a) glassy and clear but to variable degrees incipiently devitrified and commonly flow-banded, (b) holocrystalline with flow-aligned plagioclase laths and few phenocrysts, and (c) with no crystal orientation but a high content of plagioclase and orthopyroxene phenocrysts.

Juvenile ash particles include fragments of crystals and crystal clusters of mainly plagioclase and orthopyroxene. Juvenile, angular glass particles with plagioclase–orthopyroxene-dominated mineral assemblages can be divided into three groups of vertically varying proportions (Fig. 8):

Group 1 comprises particles of clear glass. Clear, highly vesicular pumice (CP, Fig. 8g) is mostly coarsely vesicular with many stretched and sheared zones, while light-gray, finely vesicular pumice (GP, Fig. 8f) contains closely packed round vesicles. Clear obsidian (CO, Fig. 8c) is mostly composed of homogeneous dense glass, but some fragments are flow-banded showing zones of different microlite content, and others have textures of sheared collapsed vesicles.

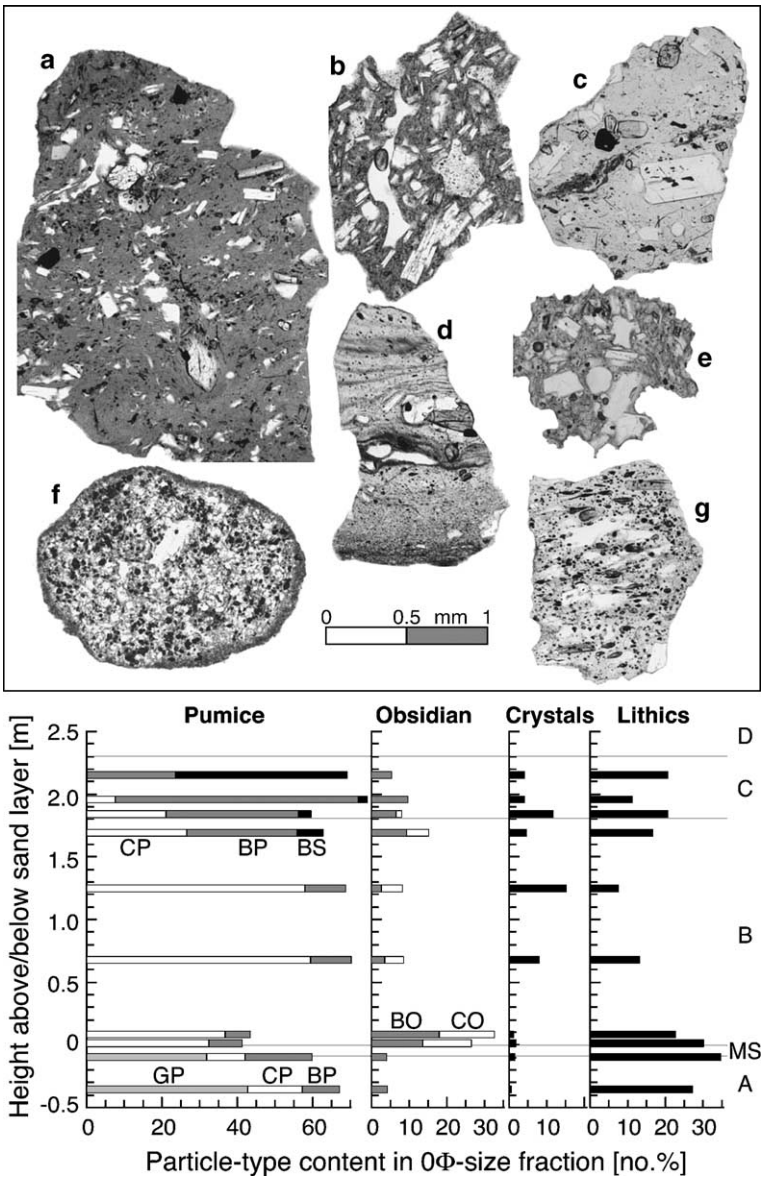

Fig. 8. Top: Photomicrographs of juvenile glass particles in the 0 Φ-ash fraction. (a) Dense brown obsidian, moderate crystal content. (b) Crystal-rich brown obsidian with incompletely collapsed, crenulate bubble. (c) Clear obsidian with opx-pl phenocrysts and central, discontinuous band of collapsed pumiceous texture. (d) Flow-banded glassy dacite lava. (e) Moderately vesicular, microlite-rich brown pumice. (f) Finely vesicular light-gray pumice with thin fine-ash rim. (g) Clear pumice with stretched vesicles. Bottom: Vertical variations in the abundance of particle types in the 0 Φ-ash fraction determined by counting in thin sections of grain mounts. Particle types are defined in the text.

Group 2 comprises particles of brown glass. A continuous range exists from light-brown highly vesicular pumice (BP, Fig. 8e), some with intense crenulate deformation, through moderate and poorly vesicular pumice to dense yellow-brown, light-brown or dark-brown obsidian fragments (BO, Fig. 8a, b), many with a collapsed-bubbles texture, containing 10–40 vol.% phenocrysts and 5–50 vol.% microlites in the glass matrix.

Group 3 comprises dark-brown to black, moderately vesicular scoria particles (BS) distinguished from BP by darker color and wider spacings between fewer vesicles.

Pumiceous particles dominate the ash fraction throughout the deposit. The very finely vesicular GP-type is limited to unit A, and commonly coated by fine ash (Fig. 8f) indicative of wet eruption conditions. The ash of unit B is dominated by clear pumice (CP) with a minor fraction of brownish pumice (BP). Both clear (CO) and brown (BO) obsidian fragments are particularly abundant in layer B1 at the base of unit B (Fig. 8). The obsidian fragments roughly covary with the lithic fragments which are most concentrated in unit A and lowermost unit B. Brown pumiceous and scoriaceous particles (BP, BS) dominate the ash of unit C (Fig. 8).

The juvenile glassy ash particles of the Mateare Tephra are texturally and compositionally (Fig. 9) distinct from glass of the underlying Xiloa and Upper Apoyeque tephras. Glass compositions of the juvenile particles correspond to matrix-glass compositions of the pumice lapilli and are shifted from the corresponding whole-rock pumice compositions due to fractionation of the plagioclase and orthopyroxene phenocrysts. The pl/opx-ratios increase from unit C through B to A (Fig. 9). The wide range in silica and alumina contents of glass in unit A and layer B1 ash particles reflects glass compositional changes in response to the presence of up to 30 vol.% pl>opx microlites. All microlite-rich particles ($Al_2O_3<13$ wt.%, $SiO_2>70$ wt.% in Fig. 9) are of the BP and BO types. Glassy flow-banded fragments of dacitic lava (stars in Fig. 9) have the same composition as ash particle types CP and CO of unit A. Considering also

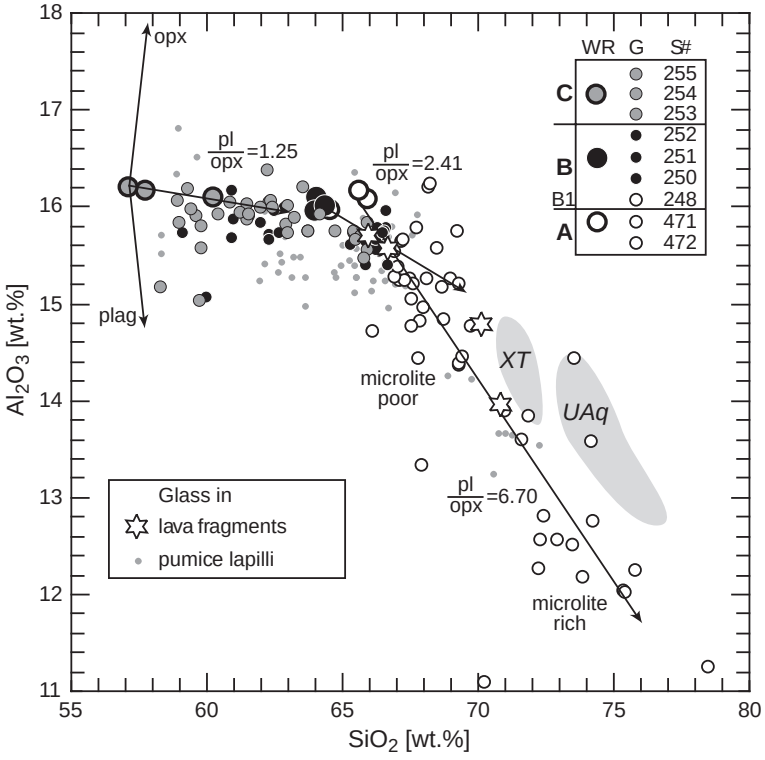

Fig. 9. Alumina versus silica variation of glass compositions of juvenile particles in the 0 Φ-ash fraction. Larger circles around 16.2 wt.% Al_2O_3 and $57<SiO_2<66$ wt.% are the corresponding pumice–lapilli whole-rock compositions, from which fractionation vectors for indicated pl/opx-ratios extend. Glass compositions of pumice lapilli (small gray dots) are shown for comparison. Dacitic lava glass fragments (stars) overlap with the Mateare rather than older tephra glass compositions (gray fields: XT=Xiloa Tephra, UAq=Upper Apoyeque Tephra).

that the textural changes from pumice through obsidian with collapsed vesicles and dense obsidian to flow-banded obsidian are continuous, at least some of the glassy lava fragments are probably of juvenile rather than lithic origin. Higher up in unit B and in unit C, no systematic compositional variation with glass color can be recognized within a given sample. Glass color thus reflects differences (e.g., oxidation, hydration) not captured by microprobe analysis.

2.6. The Mateare Tephra eruption

Well-developed bedding and moderate sorting due to significant amounts of ash in fallout unit A (Fig. 3c) indicate an initial unsteady phase of the eruption at the time when the most evolved dacitic magma was being withdrawn from the top of the reservoir. Fine-ash coatings on pumice particles and the abundance of lithic ash fragments in unit A and layer B1 (Fig. 8), a slightly reduced vesicularity of pumices (Fig. 7), and bubble growth arrested at smaller vesicle sizes in comparison to unit B indicate that the unsteady eruption behavior was caused by water accessing the conduit. The obsidian fragments, which are particularly abundant at the A/B boundary (Fig. 8), however, probably did not form as magma quenched by external water. The presence of bubble-collapse textures rather implies that this magma first vesiculated and then became permeable allowing exsolved gas to escape (cf. Westrich and Eichelberger, 1994). This is compatible with the low residual water content of 0.3 wt.% measured by infra-red spectroscopic analysis of an obsidian fragment. The clear microlite—poor and brown microlite—rich fragments had different time-lengths available for microlite growth between degassing and quenching. They possibly solidified at different depths in the conduit. The presence of flow-banded, partly devitrified dense glassy lava fragments with the same composition suggests that some of the degassed magma formed a plug or small dome at the vent. High-viscosity magma batches may therefore have partly or completely blocked the conduit near the surface and at deeper levels. Blocking of the conduit could have been another cause, in addition to groundwater access, for the unsteady nature of the early eruption phase.

In contrast, the massive and well-sorted character of units B and C (Fig. 3b) indicates a more steady plinian eruption which reached a peak discharge rate (greatest column height) after erupting the first third of unit B where the coarsest pumice occurs (Fig. 3a). During this main stage of the eruption, downward propagating withdrawal of magma from the reservoir tapped first the less silicic dacite and then the underlying andesitic magma. Once tapped the andesitic magma quickly dominated the eruption. The absence of dramatic fluctuations in eruption behavior during the change in composition can be attributed to similar viscosities and water contents of the two magmas [we estimated a viscosity ratio <3 at 4 and 5 wt.% water for andesite and dacite magma, respectively, from our unpublished chemical and thermodynamic data]. However, a transient reduction in pumice lapilli size at the B–C boundary is accompanied by a transient decrease in pumice vesicularity (Fig. 7) and an increase in lithics in the ash fraction (Fig. 8). This suggests that the discharge rate decreased temporarily facilitating the access of water to the conduit. Thereafter, the discharge rate of andesitic magma briefly returned to a forceful plinian eruption which emplaced the highly vesicular scoria in the middle part of unit C. The decrease in pumice vesicularity during the emplacement of the upper half of andesitic unit C (Fig. 7) reflects an increasing influence of invading water on the eruption dynamics. This process culminated in a fully developed phreatomagmatic eruption when the lithic-rich fallout layer D1 (Fig. 3d) was emplaced. This eruption phase re-entrained previously erupted vesicular clasts so that porosities of juvenile lapilli of layer D1 vary widely around a low average value. Layers D2 to D4 represent the terminal phase of the eruption which consisted of numerous weak phreatomagmatic explosions that emplaced wet ash fallout layers (with accretionary lapilli and vesicle tuffs) around the vent.

3. Part 2: the Mateare sand

3.1. Structure and distribution of sand layers

In most outcrops along the western shore of Lake Managua, the Xiloa and Mateare tephras are separated by a sand deposit and two erosional unconformities. The first unconformity cuts variably deep into locally reworked Xiloa Tephra (massive tuffite channel-fill),

the primary Xiloa Tephra, and even into the underlying Upper Apoyeque Tephra. This unconformity is commonly overlain by a sand deposit. In two outcrops, however, all stratigraphically intervening deposits were eroded and Mateare Tephra rests directly on top of the Upper Apoyeque Tephra. The sand deposit consists of two units separated by the second erosional unconformity.

The lower black *Xiloa Sand* is commonly well sorted and stratified, contains reworked Xiloa pumice lapilli, and is <15 cm thick unless it fills local erosional channels. The top of the Xiloa Sand is a <2-cm-thick pale gray bed of fine sand that is slightly indurated. The appearance of the Xiloa Sand is quite variable. Outside channels, well-sorted and finely planar stratified facies varies to a locally massive character (Fig. 10a) or a sequence of only moderately sorted, lapilli-rich beds (Fig. 10c). In thick channel fills, the Xiloa Sand varies from chaotically cross-bedded through finely laminated (Fig. 10d) to a massive appearance with variable contents of dispersed pumice lapilli. One channel-fill section (A93) shows four distinct layers, from cross-bedded sand with abundant fine pumice lapilli at the base through massive fine sand and a gray massive sand rich in pumice lapilli to a capping massive brown layer with little pumice. One overbank section close to the lake (Loc. Xiloa2) is composed of five layers, having massive pumiceous ash at the base, a pumice fine-lapilli layer, another ash-rich layer, a massive medium sand with

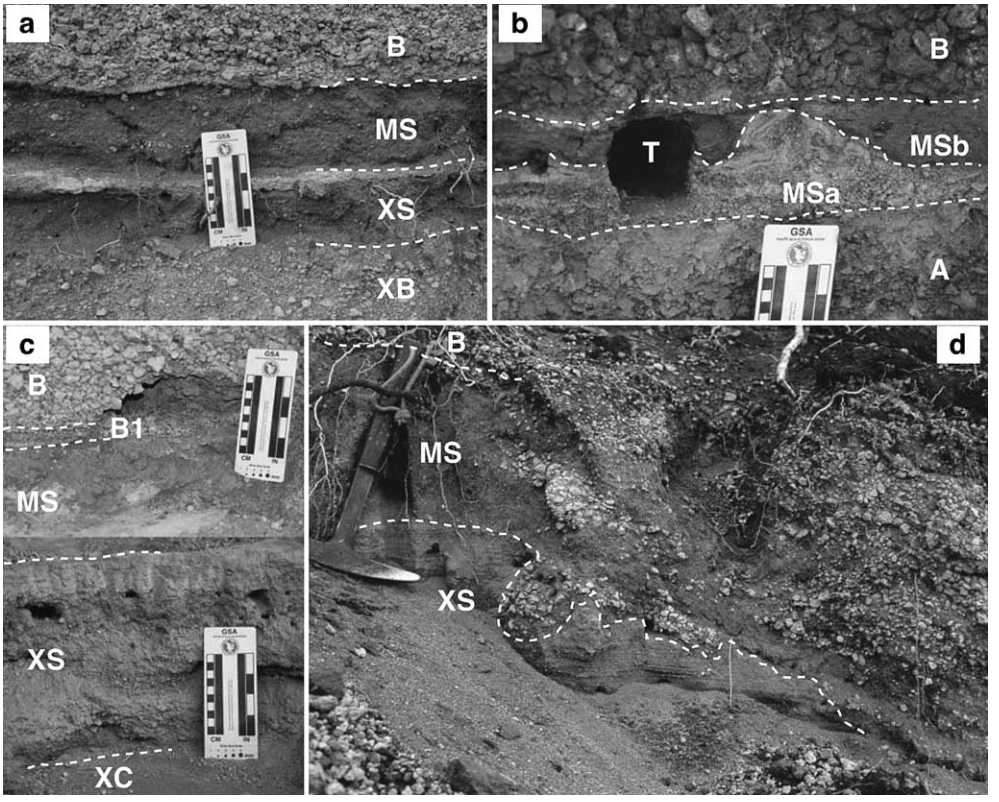

Fig. 10. (a) The fallout unit B of the Xiloa Tephra (XB) is erosively overlain (unit XC is missing) by the massive Xiloa Sand (XS) capped by a hardened light-gray fine sand layer. This is overlain by massive Mateare Sand (MS) with a wavy surface and unit B pumice fallout of the Mateare Tephra above. Loc. A119 (Fig. 1). (b) Mateare Sand composed of two layers, MSa and MSb, intercalated between fallout units A and B at Loc. A114. Note how tree stem (T, now rotten from mold) has affected MSa and MSb deposition. (c) Xiloa Sand (XS) composed of lapilli-rich beds on top of unit C of the Xiloa Tephra (XC). Overlying massive Mateare Sand (MS) has thin layer B1 on top. Loc. Xiloa2. (d) Finely planar stratified Xiloa Sand (XS) unconformably overlain by massive Mateare Sand (MS) containing numerous chaotically arranged lenses of Mateare pumice lapilli in thick channel fill at Loc. A96. Note irregular shape of the unconformity separating the sand units.

pumice lapilli, and a hardened massive silt layer at the top. Such sections show that the Xiloa Sand was emplaced by multiple depositional events.

The Xiloa Sand is commonly partly eroded at the upper contact to the overlying *Mateare Sand*. This black sand layer is typically massive, locally with internal U-shaped channel fills of the same material, and has a wavy contact to the overlying unit B fallout pumice of the Mateare Tephra (Fig. 10a). The Mateare Sand contains dispersed angular to edge-rounded gray pumice lapilli from the Mateare Tephra which are distinct from the rounded white Xiloa pumice lapilli that also locally occur in this deposit. The Mateare Sand mantles the large-scale erosional unconformities with a thickness of 2–15 cm that does not systematically vary with elevation above lake level. Instead, it fills up to 1.5-m-deep local gullies where it has a chaotic structure containing lensoid bodies of accumulated Mateare pumice lapilli (Fig. 10d). In two outcrops (A71, A114 in Fig. 1) the Mateare Sand is intercalated between units A and B of the Mateare Tephra (Figs. 3a,c, 10b); elsewhere unit A is missing. At outcrop A114, the Mateare Sand comprises two layers. The lower layer MSa, erosively overlying the primary fallout beds A1-7 (Fig. 3c), is mainly composed of pumice lapilli and ash crudely mixed with gray sand, which locally forms a distinct basal layer. It is unconformably capped by the typical massive dark sand MSb. Tree molds are common in the Mateare Sand but most abundant in outcrops that lie high above present lake level. The example in Fig. 10b shows that the presence of the tree affected the deposition of layers MSa and MSb at locality A114, 32 m above the lake. These tree molds are probably relics of driftwood washed up to near the maximum water run-up.

3.2. Sand composition

Grain size distributions of the Mateare Sand (ignoring the pumice lapilli) are unimodal (one sample has a minor second mode) with maxima between 1.5 Φ and 2.5 Φ. Median grain size Md_{Φ} = 1.8–2.2, sorting σ_{Φ} = 0.95–1.85, and fraction of grains finer than 4 Φ (1.5–17.7 wt.%) do not vary systematically with sand layer thickness or elevation above lake level. However, the sample from outcrop A114, the farthest inland and highest above lake level, is the least well sorted (1.85), contains the largest amount of fine sand (17.7 wt.%) yet has the coarsest median (1.8 Φ).

The 0 Φ-fraction of the sand contains the following particle types: (a) angular to edge-rounded highly vesicular light-gray and light-brown Mateare pumice, (b) well-rounded white Xiloa pumice, (c) dense to moderately vesicular light-brown obsidian, (d) blade-like chips of black dense obsidian containing feldspar phenocrysts, (e) dense light-gray dacite lava fragments, mostly fresh but some reddish from hydrothermal alteration, (f) feldspar and ferromagnesian crystals and crystal clusters, (g) dense dark angular fragments of mafic lava, both fresh and oxidized, some containing olivine, and (h) rounded black-brown mafic scoria particles. Proportions of these particle types vary between outcrops. Lithic fragments (g) and (h) make up 2–10% of this size fraction. Pumice types (a) and (b) amount to 20–90%, with the estimated ratio of Xiloa to Mateare pumice ranging from 0 to 1.5. The various obsidian particles dominate the non-pumiceous particle fraction.

3.3. Pumice in the sand

The bulk compositions of 30–40 g of angular to edge-rounded pumice lapilli picked from the sand at several localities vary across the compositional gap between the most evolved dacite of unit A and the less silicic dacite of unit B of the Mateare Tephra (Fig. 7), much in the same way as do samples from the base of unit B at different outcrops. The systematic zonation of the Mateare Tephra allows to use the concentration of chemical elements as an indicator of stratigraphic level in the deposit, and hence as a marker of time through the eruption. We use the concentration of Zr (Fig. 7) but analogous results are obtained with other elements.

The Zr-contents in pumice from the base of unit B differ slightly between outcrops (Fig. 11). This suggests that the change from sand to fallout emplacement at each place occurred at slightly different times. Also, Zr-content never increases above 141 ppm which means that the interval $141 < Zr < 148$ ppm (Fig. 11) represents a gap in erupted magma composition between units A and B dacites. Although the width of this gap is at the limit of analytical precision,

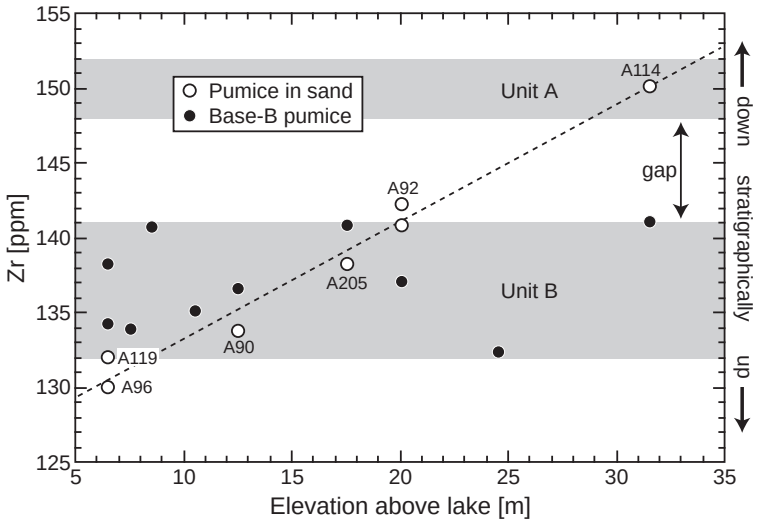

Fig. 11. Zr-concentration of pumice lapilli in the sand (white dots) and at the base of unit B (black dots) versus outcrop elevation above present lake level taken from DEM data. Gray bars indicate compositional ranges of units A and B (cf. Fig. 7). Double arrow indicates interval of Zr-concentration not observed in the erupted pumice. Labels at white dots identify localities for comparison with Fig. 5.

it systematically appears in all chemical variation diagrams (e.g., Fig. 6).

The Zr-contents in pumices in the sand increase from unit-B to unit-A concentrations with increasing elevation above lake level (Fig. 11). The bulk compositions of pumice in the sand represent mixtures of unit A and unit B pumices in different proportions. Close to the lake's shore, pumice in the sand consists almost exclusively of unit B pumice while at the highest elevation above the lake it consists exclusively of unit A pumice. In other words, the sand-forming event lasted well into the unit-B phase of the eruption at localities close to the lake shore but ended earlier at the onset of the emplacement of unit B at higher elevations above lake level.

In this context it is worth taking a second look at the thickness distribution of the Mateare Tephra. At localities such as A99 (arrow A in Fig. 5b), ~60 cm of the total deposit thickness are missing at the top due to post-eruptive erosion of unit C and part of unit B. Unit C is present, however, at localities such as A119 which lies close to the dispersal axis and yet the thickness is too small by ~50 cm (arrow B in Fig. 5b). Such localities lie at low elevations above lake level (A119, A96, A205, A90 in Fig. 5c), and pumices in the Mateare Sand here have low Zr-concentrations (Fig. 11). Reduced thicknesses of fallout unit B close to the lake are due to fallout material missing at the base of this unit. Apparently, the missing pumice has been entrained into the sand layer during the eruption. Duration and distance of transport in sand-loaded water were short since the ash and lapilli sized Mateare pumice retained angular to edge-rounded shapes. The well-rounded Xiloa pumices, on the other hand, might have been repeatedly reworked and transported if derived from eroded Xiloa Sand. Primary pumices in the Xiloa surge tuffs are, however, more rounded than the angular pumices in the Mateare Tephra fallout.

3.4. Emplacement of the sand layer

Well sorted sand layers are generally formed by aeolian or fluviatile transport or as beach sands. Aeolian transport would explain the laterally widespread distribution of the sand but can be excluded here because of the massive character and locally chaotic bedding of the sand in thick fillings of erosional channels, and the common lack of segregation of outsized pumice lapilli and of particles of greatly different density in the coarse-sand fraction. Such segregations may be inhibited during fluviatile transport under conditions of surging currents heavily loaded with sediment. Fluviatile currents directed to-

ward the lake would be capable to produce the observed erosional channels. In fact, there are numerous sandy fluviatile deposits filling erosional channels directed toward the lake in the stratigraphic succession of this area. All these deposits, however, consist of multiple beds, contain mixed volcanic clasts from a variety of source deposits, are less well sorted than the Mateare Sand, and are limited to their local channels rather than laterally widespread. A regional flash flood may explain the widespread continuous distribution of the sand. Similar to the fluviatile channel fills, however, such a flood would carry abundant detritus from the slopes of the Lomas Arribas plateau, which borders the lake west of the Chiltepe peninsula (Fig. 1) and is composed of the Mateare Formation and older volcaniclastic deposits. No such detritus is found in the Mateare Sand which is, in fact, not much different in composition from the ash fraction of the fallout deposit. This compositional feature, together with its good sorting, and widespread distribution along the shore of Lake Managua rather suggest an origin as beach sand.

Lake Managua today covers an area of ~1000 km^2, its volume is ~8 km^3, and the shoreline is ~200 km long (World Lakes Database, 2004). The average depth is 7.8 m, the maximum depth of 26 m is found near Momotombito volcanic island (Fig. 1). Until the 16th century, Lake Managua was connected to Lake Nicaragua by a broad river while overflow through the present-day Rio Tipitapa occurred only rarely in recent history. The shoreline of Lake Managua dropped from 9 m elevation above present level at 6300 a B.P. through 3 m at 1900 a B.P. to the present-day level (Cowan et al., 2002), giving a long-term average rate of −1.4 mm/a (Fig. 12a). The shoreline thus was 4–9 m higher than today when the Mateare Tephra erupted 3000 to 6000 years ago, and it was 9 m above present level when the Xiloa maar erupted at 6105 a B.P. Climatically controlled shoreline fluctuations on shorter time scales can be observed in the lake level record of INETER, Managua (Fig. 12b). Seasonal lake-level changes of ±1 m, ~2 m uprise during El Niño years, ±2 m cyclic variations with an approximately decadal period, and a transient jump to +4 m due to hurricane Mitch in 1998 occurred during the 76 years of near-continuous observation. Adding such fluctuations to shoreline 1 in Fig. 12a yields the maximum elevation to which beach and storm sand deposits can be expected. Many outcrops of the Mateare Sand, but also some of the Xiloa Sand, lie well above this level. Moreover, pumice in beach sand is typically well rounded as opposed to the angular pumice lapilli in the Mateare Sand.

The common sedimentary processes producing well-sorted sand beds thus seem inadequate to explain the character and occurrence of the Mateare Sand. Moreover, such processes would have had to fortuitously coincide with the Mateare eruption. We therefore interpret the sand layer to have been deposited by eruption-generated tsunami waves that flooded inland up to ~20 m elevation above the lake level at the time of eruption. Such waves would predominantly entrain the most recently emplaced pyroclastic material as well as pumice falling during the tsunami (i.e., the Xiloa Tephra, the Xiloa Sand, and the Mateare pumice).

Deposits from highly energetic oceanic tsunamis have been described as clast or matrix-supported conglomerates containing marine fossil detritus (Moore and Moore, 1984; McMurtry et al., 2004). On islands around Krakatau, Carey et al. (2001) observed (1) a ~30-cm-thick silt to sand bed with sharp upper and lower contacts containing dispersed pumice which they interpreted as beach material washed inland by the tsunami, and (2) overlying well-sorted, crystal and lithic-depleted lapilli layers of rounded pumice interpreted as pumice rafts stranded when the tsunami waves receded. Fine to medium carbonate sand beds with marine fossils, capped by primary fallout ash and intercalated with non-marine sediments at the coasts of western Turkey and Crete have been identified as tsunami deposits related to the Minoan eruption of Santorini (Minoura et al., 2000). The lithology of tsunami deposits is clearly controlled by the strength of the tsunami and the nature of erodable sediment in near-shore areas. In addition, the distance and direction from the vent affect the type and composition of pyroclastic material from the tsunami-forming eruption. The Mateare Sand is composed of reworked beach sand (mainly basaltic/andesitic lava sand) and dacitic fallout tephra; it is well sorted because both of these sources provided well-sorted material. The mixing, rather than segregation, of sand and low-density pumice lapilli suggests highly turbulent transport conditions that are also supported by the massive to chaotic bed structure. Juvenile pumice is not rounded

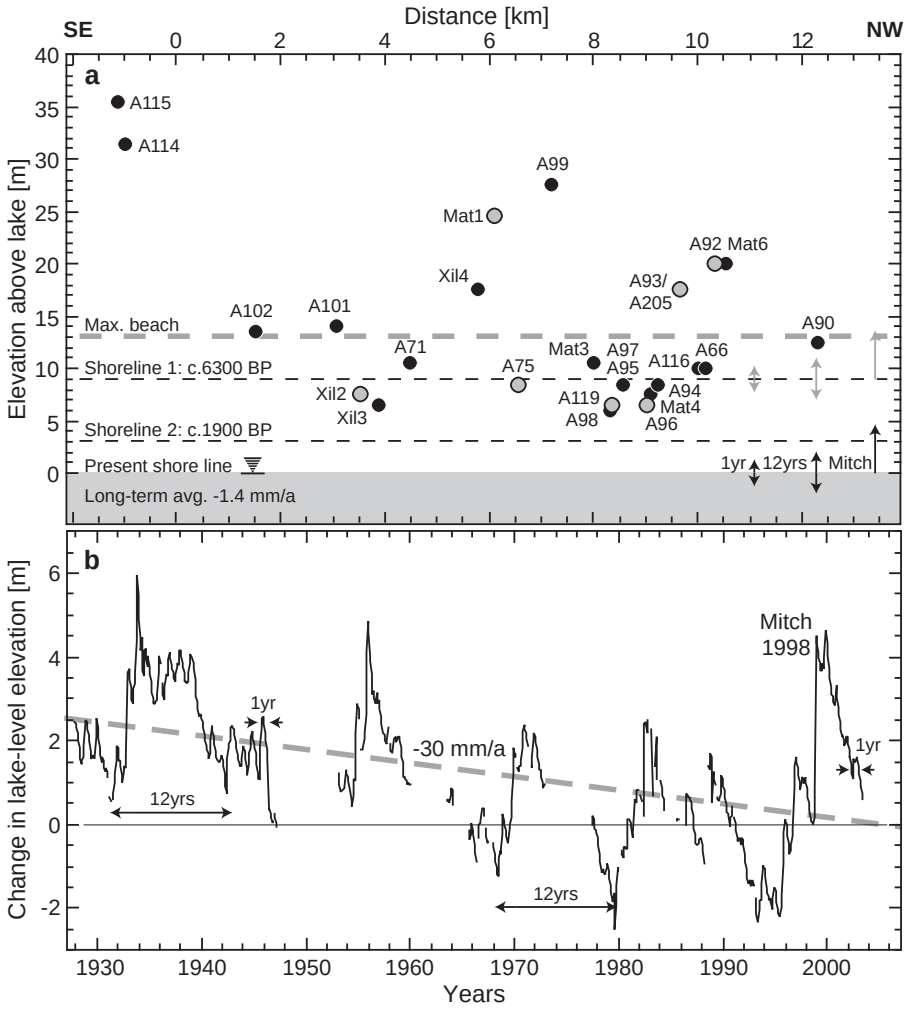

Fig. 12. (a) Position of outcrops along and above the present lake shore. Fossil shorelines 1 and 2 (dashed lines) from Cowan et al. (2002). Black dots: outcrops of the Mateare Sand. Gray dots: outcrops where the Xiloa Sand is also present. (b) Changes in lake level (relative to shore elevation 37.5 m asl in 1988 topographic map) recorded over 76 years (1927–2003) by the Direccion de Hidrografia of INETER, Managua, Nicaragua. The record shows seasonal (1 year) and near-decadal (12 years) fluctuations and a catastrophic rise after hurricane "Mitch" in 1998. These fluctuations are indicated by black arrows on the present lake level in the lower right of (a), and projected onto fossil shoreline 1 as gray arrows to derive the maximum level of beach sand formation (bold gray dashed line). The average drop-rate over the past century of about − 30 mm/a in (b) is larger than the long-term average rate of − 1.4 mm/a recorded by the fossil shorelines in (a).

because deposition rapidly followed entrainment. The fraction of juvenile tephra is high because the observed outcrops are close to, and down-wind from, the vent.

3.5. Tsunami formation during eruption

Formation of tsunamis occurred during the unsteady initial phase of the Mateare eruption. Timing of the onset of tsunami activity remains ambiguous. The position of the Mateare Sand above unit A in the two outcrops where this unit is preserved can be interpreted in two different ways: (a) tsunamis formed at the boundary between units A and B and removed previously emplaced unit A elsewhere, or (b) tsunamis formed throughout the eruption of unit A and entrained this fallout material everywhere except at these two localities where the

waves could not reach. The sand on top of unit A at outcrop A114 (Figs. 3c, 10b), presently 32 m above the lake, represents an exceptionally strong tsunami wave that entrained only unit A pumice (Fig. 11). Later waves were weaker and entrained more unit B pumice closer to the lake. This suggests waning tsunami formation when the eruption changed from its initial unsteady to its main, steady plinian phase of activity. However, compositional changes in both the sand and the local base of unit B between outcrops (Figs. 7 and 11) also reflect the influence of local topography on wave action.

Causes of eruption-generated tsunamis include subaquatic explosions and mass movements, such as volcanotectonic faulting and related earthquakes, volcano flank collapse, and invasion by pyroclastic flows. There is no geologic evidence for pyroclastic flows or flank collapse, and the lake is too shallow for tsunamigenic subaquatic mass wasting. Tectonic triggers are unlikely to continuously form tsunamis through an extended period of eruption. If the morphological depression at the northwest rim of Chiltepe peninsula was indeed the vent site (Fig. 1), it was ~6 m below lake level at the time of eruption. Tsunami formation by subaquatic explosions at 4–12 min intervals in the 40–50 m deep Karymskoye lake was observed during the 1996 surtseyan eruption. Belousov et al. (2000) describe the initiation of these tsunamigenic explosions as a bulbous updoming of a water shell up to 450 m in height within a few seconds before it got pierced by multiple ash jets and collapsed. Simultaneously, a 130-m-high wave formed around the vent and travelled radially outward at a speed of 20–40 m/s. Within 15 s after the start of the eruption, the ash fountain collapsed to form a radial base surge with a speed of 20 m/s that also contributed to wave formation.

Lacking any near-vent exposures, we can only speculate that the pulses of gas–pyroclast mixtures emitted from the vent during the unsteady initial phase of the Mateare eruption displaced the water above the vent. Eruption pulses were apparently generated by both access of water to the conduit and blasting of plugs of degassed magma (obsidian fragments), processes likely to cause overpressured erupting jets. This overpressure may have contributed to efficient tsunami formation when suddenly released at the vent exit under water. There is no field evidence to show that the Mateare eruption produced base surges but air pressure waves may have affected the fallout emplacement of the fine-lapilli layer B1 which maintains its internal stratification while pinching and swelling on the small-scale relief of the sand-layer surface. Assuming that the 3–7 cm thick fallout beds of unit A at outcrop A114 accumulated at a rate of 10^{-3} m/s typical of proximal to medial fallout (Wilson and Houghton, 2000), eruption pulses of the unsteady initial phase would have lasted 30–70 s, similar to the Karymskoye explosions. As mentioned earlier in the discussion of Figs. 5 and 11, pumice equivalent to a fallout thickness of <50 cm became trapped in the tsunamis. Using the same accumulation rate of 10^{-3} m/s, the period of tsunami formation during eruption would be constrained to <500 s. This is a minimum estimate, because breaks of unknown duration between the eruption pulses are not taken into account. Tsunami formation terminated when the purely magmatic, steady plinian eruption of unit B was established. The erupting jet was then probably no longer overpressured and there was no more impulsive displacement of water from above the vent. Moreover, a fallout tephra ring had possibly accumulated around the vent at this stage of the eruption that was sufficiently thick to keep the lake water from the vent.

4. Conclusions

The Mateare Tephra differs from the other, dacitic tephras erupted from the Chiltepe volcanic complex in being compositionally zoned from evolved dacite through less silicic dacite to andesite. The Mateare eruption evolved through three phases. The initial phase of eruption of the most evolved dacitic magma was highly unsteady due to access of external water to the conduit as well as degassed quenched magma blocking the conduit. The main steady plinian phase of the eruption involved a rapid change from dacitic to andesitic magma composition that had relatively little effect on the eruption dynamics. The Mateare eruption entered its terminal phase with a gradual change to phreatomagmatic activity of waning intensity.

Vigorous eruption pulses during the initial stage generated tsunami waves around the near-shore vent that was probably located less than 10 m below lake level. Waves flooding inland more than 20 m above lake level prevented the emplacement of fallout tephra in near-shore areas. Tephra falling on the flooded area was instead mixed with the tsunami sediment and became part of the Mateare Sand. Tsunami formation terminated when the steady plinian phase of the eruption was established.

The Mateare eruption may not have been the only tsunamigenic volcanic event at Chiltepe peninsula; occurrences of the Xiloa Sand at high elevations suggest that parts of this deposit may have been formed by tsunamis. The Chiltepe volcanic complex at Lake Managua produced six subplinian to plinian dacitic tephras over the past ~15,000 years and is therefore a likely site for a future similarly explosive eruption that could be tsunamigenic. Using the present-day average depth, $D = 8$ m, of Lake Managua to calculate the velocity of long waves as $c = (gD)^{1/2} \approx 9$ m/s, tsunami waves generated at Chiltepe by a future eruption would reach the densely populated shore at Managua City within ~15 min after initiation. The presence of active volcanoes in the vicinity of both large lakes in Nicaragua exposes the population to an elevated risk from eruption-triggered lake tsunamis. These could affect near-shore lowlands up-wind from the volcanoes which would not necessarily be seriously affected by a fallout-dominated eruption.

Acknowledgements

We thank the Dirección de Hidrografia of INETER, Managua, for supplying the lake-level record. Muchas gracias a Orlando Membreño, Guillermo Rocha, Antonio Lopez, Felix Henrìquez y Pedro Pérez por sus ayuda en el campo. Kristina Bernoth and Kerstin Schirmer helped with sample preparation and grain-size analyses. Dagmar Rau performed the XRF analyses and Mario Töner assisted with the microprobe analyses. Radiocarbon dating was done by the Leibniz Laboratory for Age Dating and Isotope Research at Kiel University. This publication is contribution no. 68 of the Sonderforschungsbereich 574 “Volatiles and Fluids in Subduction Zones” at Kiel University.

References

Belousov, A., Voight, B., Belousova, M., Muravyev, Y., 2000. Tsunamis generated by subaquatic volcanic explosions: unique data from 1996 eruption in Karymskoye Lake, Kamchatka, Russia. Pure Appl. Geophys. 157, 1135–1143.

Bice, D.C., 1985. Quaternary volcanic stratigraphy of Managua, Nicaragua: correlation and source assignment for multiple overlapping plinian deposits. Geol. Soc. Am. Bull. 96, 553–566.

Bourgeois, J., Petroff, C., Yeh, H., Titov, V., Synolakis, C.E., Benson, B., Kuroiwa, J., Lander, J., Norabuena, E., 1999. Geologic setting, field survey and modeling of the Chimbote, northern Peru, tsunami of 21 February 1996. Pure Appl. Geophys. 154, 513–540.

Carey, S., Morelli, D., Sigurdsson, H., Bronto, S., 2001. Tsunami deposits from major explosive eruptions: an example from the 1883 eruption of Krakatau. Geology 29, 347–350.

Cowan, H., Prentice, C., Pantosti, D., de Martini, P., Strauch, W., 2002. Late Holocene earthquakes on the Aeropuerto Fault, Managua, Nicaragua. Bull. Seismol. Soc. Am. 92, 1694–1707 (workshop participants).

De Lange, W.P., Prasetya, G.S., Healy, T.R., 2001. Modelling of tsunamis generated by pyroclastic flows (ignimbrites). Nat. Hazards 24, 251–266.

Freundt, A., 2003. Entrance of hot pyroclastic flows into the sea: experimental observations. Bull. Volcanol. 65, 144–164.

Freundt, A., in press. Entrance of hot pyroclastic flows into the sea: Experimental tsunami formation. Bull. Volcanol.

Harbitz, C.B., 1992. Model simulations of tsunamis generated by the Storegga slides. Mar. Geol. 105, 1–21.

Keating, B.H., McGuire, W.J., 2000. Island edifice failures and associated tsunami hazards. Pure Appl. Geophys. 157, 899–955.

Latter, J.H., 1981. Tsunamis of volcanic origin: summary of causes, with particular reference to Krakatoa, 1883. Bull. Volcanol. 44, 467–490.

McCoy, F.W., Heiken, G., 2000. Tsunami generated by the Late Bronze Age eruption of Thera (Santorini), Greece. Pure Appl. Geophys. 157, 1227–1256.

McMurtry, G.M., Fryer, G.J., Tappin, D.R., Wilkinson, I.P., Williams, M., Fietzke, J., Garbe-Schönberg, D., Watts, P., 2004. Megatsunami deposits on Kohala volcano, Hawaii, from flank collapse of Mauna Loa. Geology 32, 741–744.

Miller, D.J., 1960. Giant waves in Lituya Bay, Alaska. U.S. Geol. Surv. Prof. Paper 354-C, 1–86.

Minoura, K., Imamura, F., Kuran, U., Nakamura, T., Papadopoulos, G.A., Takahashi, T., Yalciner, A.C., 2000. Discovery of Minoan tsunami deposits. Geology 28, 59–62.

Moore, J.G., Moore, G.W., 1984. Deposit from a giant wave on the island of Lanai, Hawaii. Science 226, 1312–1315.

Perez, W., Freundt, A., in press. The youngest highly explosive basaltic eruptions from Masaya Caldera Complex (Nicaragua): Stratigraphy and hazard assessment. In: Rose, W.I., et al. (Eds.) Volcanic hazards in Central America. Geol. Soc. Am. Spec. Publ.

Self, S., Rampino, M.R., Newton, M.S., Wolff, J.A., 1984. Volcanological study of the great Tambora eruption of 1815. Geology 12, 659–663.

Sigurdsson, H., Carey, S.N., 1989. Plinian and co-ignimbrite tephra fall from the 1815 eruption of Tambora volcano. Bull. Volcanol. 51, 243–270.

Sussman, D., 1985. Apoyo Caldera, Nicaragua: a major Quaternary silicic eruptive center. J. Volcanol. Geotherm. Res. 24, 249–282.

Vallance, J.W., Schilling, S.P., Devoli, G., 2001. Lahar Hazards at Mombacho Volcano, Nicaragua. 01-457. U.S. Geological Survey, Vancouver WA.

Voight, B., Glicken, H., Janda, R.J., Douglass, P.M., 1981. Catastrophic rockslide avalanche of May 18. In: Lipman, P.W., Mullineaux, D.R. (Eds.), The 1980 Eruptions of Mount St. Helens, Washington, U.S. Geol. Survey Prof. Paper, vol. 1250, pp. 347–377.

von Huene, R., Ranero, C.R., Watts, P., 2003. Tsunamigenic slope failure along the Middle America Trench in two tectonic settings. Mar. Geol. 3415, 1–15.

Waythomas, C.F., Neal, C.A., 1998. Tsunami generation by pyroclastic flow during the 3500-year B.P. caldera-forming eruption of Aniakchak volcano, Alaska. Bull. Volcanol. 60, 110–124.

Westrich, H.R., Eichelberger, J.C., 1994. Gas transport and bubble collapse in rhyolitic magma: an experimental approach. Bull. Volcanol. 56, 447–458.

Williams, S.N., 1983. Plinian airfall deposits of basaltic composition. Geology 11, 211–214.

Wilson, C.J.N., Houghton, B.F., 2000. Pyroclast transport and deposition. In: Sigurdsson, H., et al., (Eds.), Encyclopedia of Volcanoes. Academic Press, San Diego, pp. 545–554.

World Lakes Database, 2004. Accessible at www.ilec.or.jp.